Combustion and Flame 257 (2023) 112993

Contents lists available at ScienceDirect

Combustion and Flame

journal homepage: www.elsevier.com/locate/combustflame

On the structure of buoyant fires with varying levels of fuel-turbulence

Tony Xiao [a], Vinny Gupta [a,*], Andrew R.W. Macfarlane [a], Callum Kennedy [a], Matthew J. Dunn [a], Agisilaos Kourmatzis [a], José L. Torero [b], Assaad R. Masri [a]

[a] School of Aerospace, Mechanical and Mechatronics Engineering, The University of Sydney, Darlington, NSW 2008, Australia
[b] Department of Civil, Environmental and Geomatic Engineering, University College London, London, WC1E 6BT, United Kingdom

ARTICLE INFO

Article history:
Received 13 February 2023
Revised 24 July 2023
Accepted 26 July 2023

Keywords:
Fire dynamics
Buoyant turbulent flames
Laser-induced fluorescence
Flame pinch-off

ABSTRACT

This paper employs a novel burner to study the effects of fuel-generated turbulence on the spatial and temporal structure of buoyant turbulent diffusion flames which are representative of large fires. Fuel-turbulence levels are increased using a perforated plate that issues high-velocity jets, enabling shearing of the fuel stream. The perforated plate may be recessed to control the turbulence level at the jet exit plane. It is shown that the exit plane axial velocity fluctuations can be increased from 0.135 m/s to 1.813 m/s. Varying the levels of fuel-turbulence in the burner allows for the control of key processes defining buoyant fires such as the spatial and temporal flame structure and flame instability modes. These processes are characterised by high-speed simultaneous imaging of planar laser-induced fluorescence of the OH radical (OH-PLIF) and Mie scattering from soot particles. Increasing the fuel-turbulence level deforms the flame, which promotes non-radial lateral entrainment into the flame sheet. This results in a sharp increase in the tilting of the near-field flame sheet along the vertical flame axis. Strong angular entrainment forces are shown to overcome the diffusive and thermal expansive forces at the flame neck, which leads to a strained asymmetric sinuous flame pinch-off instability, followed by separation of the flame base. Sinuous pinch-off instabilities occur at a greater frequency than the symmetric varicose pinch-off instabilities observed for flames with low fuel-turbulence. The asymmetric stretching of the flame neck inhibits the formation of the classical puffing instability formed with an axisymmetric plume that defines classically buoyant flames. Probability density functions calculated for the flame front curvature and flame surface area are shown to monotonically broaden in the near-field region of the flame due to lateral entrainment effects. The transition to buoyancy-driven turbulence also shifts to an increasingly more upstream location. This burner, with its well-defined boundary conditions and novel data, forms a platform for advancing capabilities to model complex fire phenomena including turbulence-buoyancy interactions.

1. Introduction

The structure and heat transfer mechanisms governing the burning behaviour of fires are the result of coupled interactions between energy release and the fire-induced flow fields arising from buoyancy forces. At realistic length scales, fire dynamics are defined by a complex three-dimensional interaction of turbulent mixing, mass transport, flame radiation, gas-phase chemistry, and soot formation and oxidation processes that operates in a volume with length scales that can be in the order of several metres [1]. The outcome of these complex coupling processes may be interpreted through macroscopic features of a fire such as the flame height [1], entrainment rates [2], thermal feedback [3], burning rates [4], global radiative fractions [5], and soot volume fractions [3,5], all of which typically serve as integral inputs/outputs of computational predictive models [6]. These macroscopic features are coarsely characterised and heavily empirically driven, and this is beneficial for fast computations of fire behaviour over a broad range of mesh sizes that is amenable to resolving fire problems. However, one drawback to the empirical nature of these estimations is that they are often scenario specific hence limiting the ability of such models to generalise [7]. To improve the predictive capabilities of fire models, it is important to better resolve the different processes locally. This requires carefully designed experiments with well-posed boundary conditions and detailed and quantifiable outputs. This paper is a first step towards achieving this objective.

* Corresponding author.
E-mail address: vinny.gupta@sydney.edu.au (V. Gupta).

https://doi.org/10.1016/j.combustflame.2023.112993

Nomenclature

Fr_f	Buoyancy-momentum flame Froude Number
u_s	Nozzle fuel flow velocity
S	Air to fuel mass stoichiometric ratio
ρ_s	Fuel density at the nozzle
ρ_o	Ambient air density
$\overline{\Delta T_{fa}}$	Modified mean peak flame temperature rise
T_o	Ambient temperature
g	Gravitational acceleration
d_s	Nozzle diameter
HRR	Heat release rate
ΔH_c	Heat of combustion
$\dot{m}_f$	Fuel mass flow rate
σ	Cross-correlation factor
L_R	Plate recess distance
f_p	Puffing frequency
ϵ	Turbulence intensity
κ	Flame front curvature

Over the past few decades, there has been a systematic push to validate the sub-models of modern computational fluid dynamics codes through the development of statistically resolved databases that are amenable to validating turbulent flows [8], gas-phase temperature fields [8–10], radiative emissions [3] and soot formation [10–12]. These databases provide valuable temporal and spatially resolved profiles of key quantities such as the simultaneous LII/CARS measurements by Frederickson et al [13] and Kearney et al [14], which deliver joint statistical data on key quantities such as gas-phase temperature and soot volume fraction. These kinds of databases have facilitated an improved phenomenological understanding of buoyant turbulent fires; however, they are generally limited by the lack of resolution of the complex turbulence intensity fields. This is because the turbulence level is difficult to parameterise since turbulence is constrained to the air-side strain rate, which is governed by the fuel size, mass transfer number, and boundary condition for condensed fuels, or the fuel injection rate for gaseous fuels. In both cases, turbulence is generated by the buoyancy forces acting along the air entrainment region axis and is therefore not particularly amenable to being controlled and parameterised experimentally. Moreover, canonical buoyant flames used as model benchmarks consist of porous sand and sintered bronze burners (e.g. UMD Line Burner [15], and the FM Global Ethylene Burner [11,16]) and liquid pool fire experiments (e.g. Weckman and Strong [8], NIST Pool Fires [17], and Sandia's FLAME facility [18]). These types of experiments create complexities and couplings at the fuel surface that are difficult to model and require either the resolution of species transport in a porous media (sand and sintered bronze burners) or quantification of the surface energy balance (pool fires). The latter is particularly challenging as the flame-to-surface feedback requires a detailed resolution of convective and radiative transport across very small length scales, which is often not amenable for validation studies due to limitations in the available data as sophisticated near-wall diagnostics are required [19]. Instead of modelling mass transport at the surface, empirical wall functions developed for non-reacting flows are usually employed, carrying significant limitations and uncertainties when extrapolated to fire scenarios [6]. Thus, the surface boundary condition that describes the local mass transport of fuel from such fire sources is poorly conditioned to validate the complex sub-models needed to scale-up fire processes [20].

High-fidelity measurements characterising both spatially and temporally the flame structure of buoyancy-driven flames at the scales of fires are not readily available in the literature [21]. This is largely owing to the sensitivity of a buoyant turbulent flow that forms above the condensed fuel surface to the fuel boundary conditions and other parameters. An example of this complexity is demonstrated by flow visualisation measurements for the piloted ignition of an oil slick by Wu et al [22]. These experiments show a distinct increase in the turbulence level above the condensed fuel upon the inclusion of a flush floor surrounding the heated fuel tray as observed by the absence of symmetric eddy structures observed for an isolated fuel tray. Such observations are emblematic of realistic fire scenarios at larger scales and demonstrate the importance of developing experiments at a canonical scale that have well-defined boundary conditions yet can generate controlled turbulence levels that are typical of large-scale fires. This has been identified as a major gap in the literature [21] and has therefore motivated the development of the burner proposed here which stabilises buoyant turbulent diffusion flames, with a simple mechanism for introducing and controlling the level of fuel-turbulence. The burner utilises a perforated plate that issues small jets of fuel that generate high shear and high levels of turbulence. The plate may be recessed into an outer jacket to control the level of turbulence so that, for the same bulk fuel velocity, different recess distances will result in different levels of turbulence at the burner's exit plane. This is a key feature that enables the generation of high levels of turbulence in a low-mean-velocity buoyant jet and this is different from the burner of Zhang et al [23] who used a porous plate at the burner exit plane.

This burner introduced here enables a study of turbulence-buoyancy interaction in flames where fuel-turbulence is well controlled and boundary conditions are well-posed and easily modelled. The resulting database complements existing literature and lays a platform for future quantitative measurements and model development. Fuel injection rates are kept sufficiently low to ensure buoyancy-driven flames. The turbulence generated from the recessed plate at the burner exit plane is characterised using Laser Doppler Velocimetry (LDV) of a non-reacting cold flow. The effect of the induced fuel-side turbulence on the temporal and spatial structure of the fire is studied through high-speed imaging of planar laser-induced fluorescence (PLIF) of the OH radical and Mie scattering of soot (OH-PLIF-Scattering).

2. Experimental setup and diagnostics

2.1. Burner design

The burner, shown schematically in Fig. 1, consists of a tube 35 mm ID (2.5 mm wall thickness) that issues the fuel jet to form simple buoyant flames (label 1 in Fig. 1a). The burner is made of brass and the fuel employed is compressed natural gas (CNG, which consists of 88.8% CH_4, 7.8% C_2H_4, 1.9% CO_2 and 1.2% N_2). The burner assembly is positioned into a wind tunnel with co-flow to stabilise the flame.

The novelty of the burner lies in the inclusion of a perforated plate that can be recessed within the 35 mm outer jacket. The perforated plate, shown in Fig. 1a (label 2) and Fig. 1b, has a thickness of 8 mm and 25 holes with a diameter of 1 mm. The perforated plate can be mounted on a sliding mechanism (label 3 in Fig. 1a), which can be recessed into the outer jacket up to a distance L_r = 100 mm upstream of the burner exit plane. The perforated plate generates high-velocity jets that issue from the small holes to create high shear and hence large fuel-turbulence levels at the burner exit plane. Since this burner operates by introducing shear-driven turbulence, the turbulence level is therefore controlled by increasing the fuel flow rate as it enhances shearing within the fuel flow. Also, for the same fuel flow rate, the turbu-

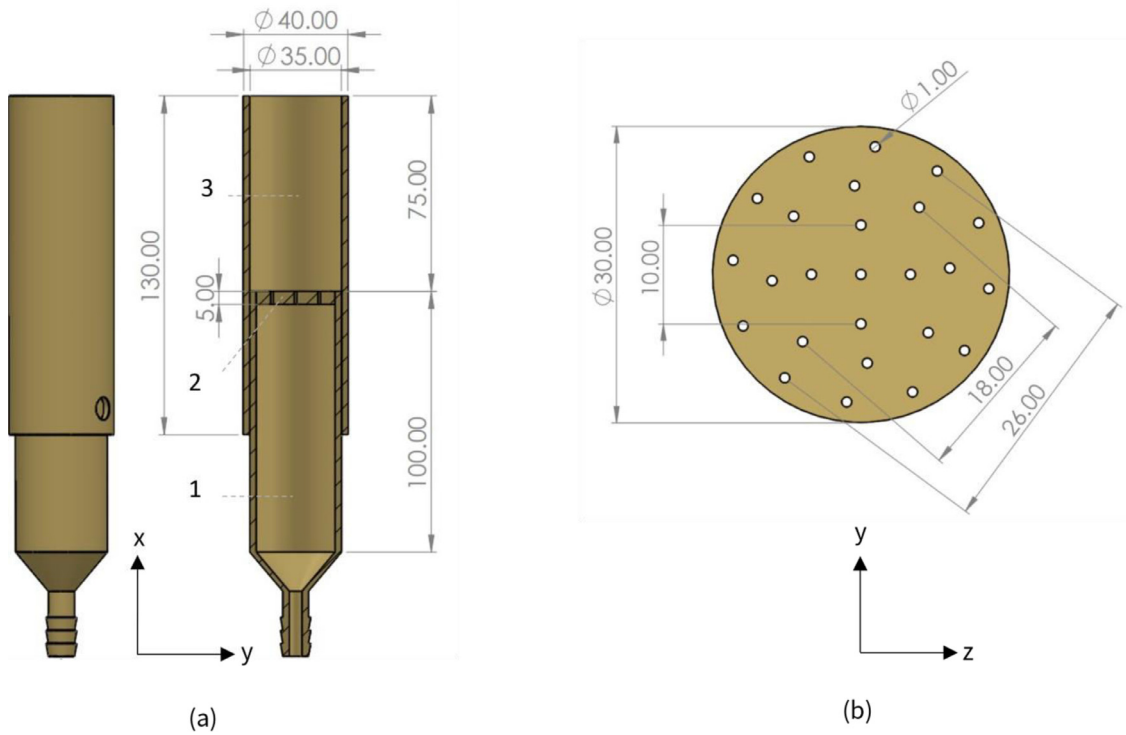

Fig. 1. Schematic of the (a) burner assembly and (b) turbulence generator, all dimensions in millimetres.

lence level at the jet exit plane can be controlled by recessing the plate within the annulus. The burner is manufactured from brass and the fuel used in this study is compressed natural gas (CNG, which consists of 88.8% CH_4, 7.8% C_2H_4, 1.9% CO_2 and 1.2% N_2). Noting that there are numerous definitions of the Froude number, the one listed in Eq. (1) is used here for convenience. Both the Froude number and heat release rate (Eq. (2)) are controlled by the fuel mass flow rate. The burner assembly is positioned in a wind tunnel with co-flow to stabilise the flame.

$$Fr_f = u_s / \left[(S+1)^{\frac{3}{2}} \left(\frac{\rho_s}{\rho_o} \right)^{\frac{1}{4}} \left(\frac{\overline{\Delta T_{fa}}}{T_o} g\, d_s \right)^{\frac{1}{2}} \right] \quad (1)$$

$$\dot{Q} = \Delta H_c \dot{m}_f \quad (2)$$

The fire Froude number shown in Eq. (1) characterises the aerodynamic effects with respect to the diameter of the burner exit plane [24]. A description of the various parameters is given in the nomenclature. The Froude number determines whether a flame may be classified as a buoyant jet ($Fr_f \geq 2$), pool fire ($Fr_f \geq 0.1$) or a mass (percolating) fire ($Fr_f \leq 0.1$) [16,21]. The fuel injection rates are selected to ensure that Froude numbers for the flames studied lie solely within the pool fire regime defined by Delichatsios [25]. The burner operating conditions are optimised by varying the fuel flow rates, air co-flow rate and plate recess distance to ensure that flame lift-off or blow-off does not occur. The burner operating limits are then selected based on a stability mapping for flame lift-off. The probe volume is kept 1.5 m below the exhaust duct in an open atmosphere to ensure that the exhaust does not influence the experiment. The co-flow is supplied by a wind tunnel operating under standard atmospheric conditions. The wind tunnel exit velocity was set to approximately 0.2 m/s. The heat release rate (HRR) of the fuel is estimated by assuming complete combustion for CNG ($\Delta H_c \approx 50$ MJ/kg). To demonstrate the utility of the burner, a single plate recess distance of $L_r = 75$ mm is selected and studied for the five flames of varying turbulence levels. The corresponding flow rate, bulk velocity, Reynolds, Froude numbers and dimensionless heat release rates [26] are shown in Table 1.

Table 1
Burner operating conditions for the different flames were sorted by increasing turbulence levels (Table 2).

Flame	Turbulence Generator	$\dot{Q}$ (kW)	$\dot{m}_f$ (L/min)	V (m/s)	Re	Fr_f	$\dot{Q}^*$
F1	No	10	18.3	0.317	678	0.0064	31.75
F2	Yes	10	18.3	0.317	678	0.0064	31.75
F3	Yes	20	36.6	0.634	1357	0.0127	63.51
F4	Yes	30	54.9	0.951	2034	0.0191	95.26
F5	Yes	40	73.2	1.268	2715	0.0254	127.0

2.2. LDV measurements

A commercial LDV system (TSI Model FSA 4000) was used for the single-point measurements of velocity and turbulence level. An Argon-ion laser feeds a two-channel fibre optics assembly to the transmitter while the 300 mm focal length receiver was positioned in a 31° forward scattering configuration with a 3.74 μm fringe spacing. Two pairs of beams with wavelengths 514.5 nm and 488.0 nm are used for measuring the axial and radial components of velocity, respectively. Built-in probe volume correction (PVC) in the software (FlowSizer) has been implemented to correct for lower detectability of small particles at the edge of the probe volume. Point measurements of the mean and rms axial velocity were taken radially along the exit plane of the burner for a non-reacting flow, with similarity of the bulk volumetric flow rates maintained.

The burner was seeded with an ultrafine mist generated from an ultrasonic nebuliser of water doped with a small concentra-

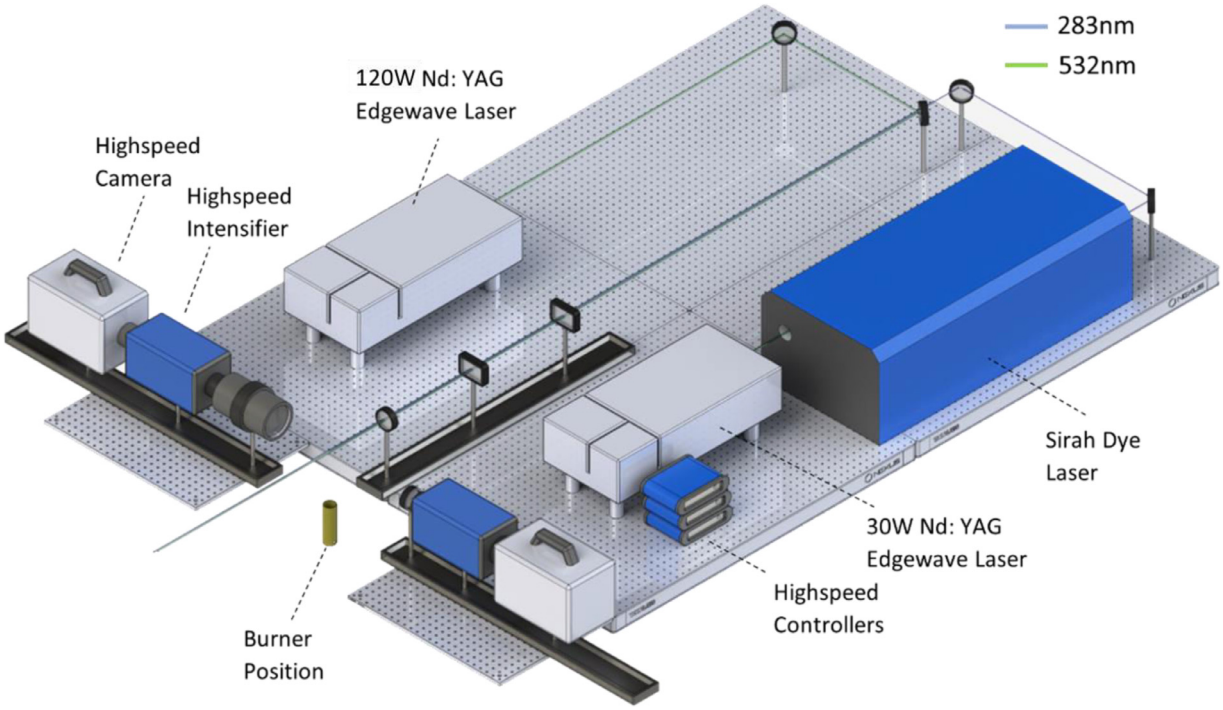

Fig. 2. Experimental and laser setup for the simultaneous high-speed imaging of OH-PLIF and Mie scattering of soot.

tion of sodium bicarbonate powder ($NaHCO_3$). Once the droplets form during primary atomisation and undergo thermal expansion and evaporation, the small $NaHCO_3$ crystals suspended in the flow enable a sufficient number density of droplets/crystals needed to resolve the flow field at the burner exit plane. This doping mechanism was particularly necessary for larger flow rates as droplet evaporation is greatly enhanced due to the larger streamwise velocity, and therefore no water droplets were detected at the burner exit plane. The droplet-particle flow exhibited a monomodal diameter distribution with a geometric mean (d_{10}) at approximately 1 μm, meaning that the Stokes number of the droplets is small. Therefore, the droplets can be assumed to follow the flow field generated inside the burner assembly. Careful attention was required to ensure that blockage of the holes in the perforated plate and the flow straightening mesh did not occur, as this was found to influence the results heavily. To account for this, the burner was frequently purged to remove any blockages. Data was sampled for approximately 30 s, with data acquisition rates typically ranging from 5000 Hz in the centre of the burner exit plane and 200 Hz towards the edges of the flow.

2.3. Joint high-speed imaging of OH-PLIF and soot scattering

The optical setup employed for the joint high-speed imaging of OH radicals and soot Mie scattering is shown in Fig. 2. Soot Mie scattering at 532 nm is generated by a frequency doubled 120 W Nd:YAG laser (Edgewave HD30II-E) operating at a repetition rate of 10 kHz and a 9 ns pulse duration. The vertically polarised 532 nm Mie scattering beam is attenuated to ~1 mJ/pulse to avoid excessive scattering signal levels and laser-induced incandescence by a combination of a half-wave plate and a thin film polarizer. For OH fluorescence excitation, a frequency doubled 30 W Nd:YAG laser (Edgewave InnoSlab IS8II-E) operating at a frequency of 10 kHz and a wavelength of 532 nm, is used to pump a dye laser (Sirah Allegro) using Rhodamine 6G dissolved in ethanol. The dye laser beam is tuned such that after the frequency doubling the UV wavelength corresponds to the $Q_1(6)$ OH A-X (1,0) transition at 283.01 nm with ~100 µJ/pulse energy and 10 ns pulse duration. After correction for the different focal lengths of the UV and the 532 nm beams, the two beams are overlapped, expanded in the vertical direction and passed through a 300 mm focal length cylindrical lens to form the laser imaging sheet. The combined laser sheets at the measurement zone are approximately 50 mm in height with a nominal thickness of 200 μm.

The soot Mie scattering signal is collected orthogonally to the laser sheet with a 50 mm $f_\# = 1.8$ Nikkor lens connected to a two-stage high-speed intensifier (LaVision HighSpeed IRO) and the subsequent image is recorded by a high-speed CMOS camera (LaVision High-Speed Star 6). Interferences from flame luminosity are removed using a 10 nm FWHM, 532 nm bandpass filter, combined with a 200 ns intensifier gate. The OH-PLIF signal is collected orthogonally to the laser sheet on the opposite side to the Mie scattering collection system, with a 96 mm $f_\# = 1.65$ UV lens (2xLAPQ/APMQ-300.0–60.0-PM CVI Laser Optics) [27], coupled to an identical high-speed intensifier and high-speed CMOS camera as the Mie scattering collection system. The fluorescence from the OH A-X (1,1) and (0,0) bands are collected, while simultaneously blocking laser scattering and flame luminosity using a 200 ns intensifier gate and a combination of filters that includes a 300 nm long-pass filter, a 15 nm FWHM 315 nm bandpass filter and a 1 mm thick UG11 coloured glass filter. The UV OH PLIF beam is delayed by 200 ns from the 532 nm Mie scattering beam to avoid any cross talk between the two processes. Both cameras are set to acquire images at 250 Hz, a much lower rate than the laser frequency of 10 kHz to ensure a greater sampling time of the relatively low-speed buoyant flames examined in this study, yet still sufficient to temporally resolve the flame structures between successive images. Multiple calibration images are taken throughout the experiment to correct for variations in camera background and noise, optical throughput uniformity and laser sheet profiles, with the appropri-

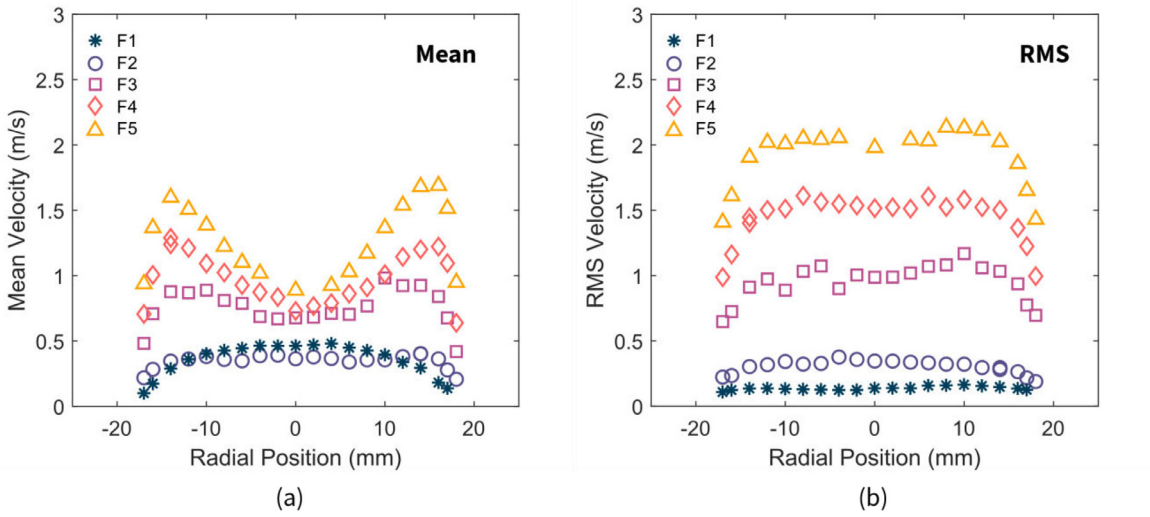

Fig. 3. Burner exit plane velocity profiles (mean and rms) for all the flames.

ate corrections applied in post-processing. A 3 × 3 median filter followed by a 5 × 5 Gaussian filter is applied to images after background subtraction to minimise the effects of noise. Both cameras have been de-warped using a grid calibration plate applying a 3rd order polynomial geometric transformation [28] resulting in a rms mapping error of less than 1 pixel over the region of interest. The spatially mapped cameras together have a projected pixel size of 0.5 mm/pixel for the OH camera and 0.4 mm/pixel for the soot scattering camera. The de-warped images have a maximum window size of 65 mm (height) by 130 mm (width). Both the PLIF-OH and Mie scattering of soot images have a threshold applied zeroing all pixels below that of 10 counts and 5% of the maximum counts.

2.4. Validation of the turbulence-generating mechanism

This section reviews the association between fuel-turbulence and HRR both with and without the turbulence-generating plate to ensure increased fuel-turbulence levels are not solely a function of increasing HRR but a function of the burner design. Figure 4 shows the burner exit plane fuel-turbulence levels ϵ for all HRRs studied herein using Eq. (4). It is clearly shown that without the perforated plate, increases in fuel-turbulence levels are minor as the HRR increases, scaling linearly from 0.135–0.483 m/s. Whereas, with the addition of the plate, fuel-turbulence levels increase substantially from 100% to 300% for the 10 kW to 40 kW flames respectively.

3. Experimental results

Results are presented in three sections starting with the flow fields measured at the jet exit plane of non-reacting cases. This is followed by a detailed qualitative description of flame characteristics with increasing levels of turbulence. The third section shows a more detailed analysis of the temporal structure of the flame and the imaged OH layers. The final section discusses the spatial angular orientations of the OH layers.

3.1. Burner velocity and turbulence profiles

Radial profiles of the mean axial velocity and RMS velocity fluctuations measured at the burner exit plane for the five cases studied under a cold non-reacting flow are presented in Fig. 3. The mean burner exit velocity profiles for each flame case are

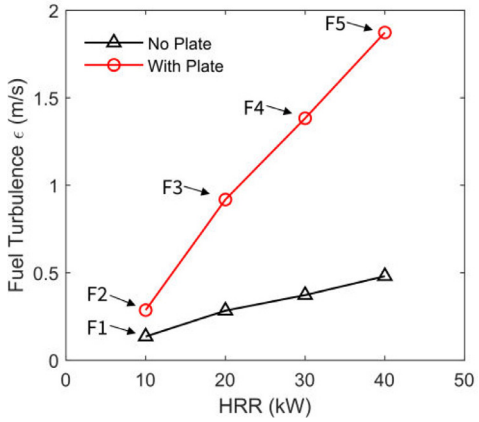

Fig. 4. Exit plane fuel-turbulence for all HRR with and without the turbulence generation plate.

shown in Fig. 3a, while the profiles for the RMS velocity are shown in Fig. 3b. The presented RMS values, u_i', are computed as per Eq. (3). The addition of the perforated plate changes the mean and rms axial velocity profiles considerably. The rms fluctuations range from 0.12 m/s for F1 to 2 m/s for F5. Upon increasing the turbulence levels, Fig. 3a shows an increasingly distinct "M" shaped mean velocity profile with peak velocities occurring near the wall for the higher turbulence F3-F5 cases. In each flame presented, shear-driven turbulence is raised by increasing the bulk fuel flow rate, with the exception being between F1 and F2, which possess the same bulk mass flow rates to highlight the effect of the turbulence-generating plate on the profile. The resultant velocity distributions shown are a combination of both an increase in overall bulk flow velocity and the subsequent enhancement of shear turbulence due to the addition of the plate (F2–F5). Previous studies have also shown similar "M" shaped velocity profiles for high blockage ratio perforated plate turbulence generation [29,30]. The increase in the fuel-turbulence level is associated with the design of the perforated plate, which demonstrates that the burner is performing as intended.

The flames have been sorted (F1–F5) by increasing levels of fuel-turbulence. A single metric for the inlet turbulence level to categorise each flame has been developed, termed the fuel-

Table 2
Bulk fuel velocity, bulk fuel-turbulence levels and centerline Integral length and time scales.

Flame	V (m/s)	T_f (s)	l_0(m)	Fuel-turbulenceϵ (m/s)
F1	0.317	1.17E−02	5.14E−03	0.135
F2	0.317	1.48E−02	5.12E−03	0.283
F3	0.634	8.15E−03	6.49E−03	0.918
F4	0.951	4.59E−03	4.94E−03	1.383
F5	1.268	4.18E−03	4.91E−03	1.873

turbulence, ϵ (m/s), which is defined per Eq. (4) and shown for each flame in Table 2. The fuel-turbulence, ϵ, is defined by a discretised radial integral of the measured velocity RMS u_i' (Eq. (3)) over r_i the radius of the discretised burner exit plane. This formulation takes the summation of the radial component (u_{x_i}) orthogonal to the burner exit plane and the azimuthal component (u_{y_i}).

$$u_i' = \sqrt{u_{x_i}^2 + 2u_{y_i}^2} \tag{3}$$

$$\epsilon = \sum_{i=0}^{n} u'_i\left(r_{i+1}^2 - r_i^2\right)/r_n^2 \tag{4}$$

The LDV measurements are exploited to calculate the integral length scale (η) at the exit plane from the single-point Eulerian autocorrelation function $\rho(\tau)$. This assumes Taylor's frozen turbulence hypothesis and the integration of $\rho(\tau)$ to obtain an integral time scale (T_f) using Eq. (5), which is multiplied by the local mean velocity to obtain an approximate integral length scale. Due to the random sampling nature of the LDV data, the slotting technique by Nobach [31] is used to calculate the single-point Eulerian autocorrelation function.

$$T_f = \int_0^\infty \rho(\tau)d\tau \tag{5}$$

The integral time scales (T_f) and integral length scales (l_0) of the axial velocity component of all flames are presented in Table 2. The time scales decrease with increasing levels of fuel-turbulence, suggesting an increase in the turnover rate of turbulent structures. The length scales, however, seem to be very similar for all cases, this indicates that the size of the turbulent structures is perhaps solely governed by the size of the holes in the perforated plate, resulting in similar integral length scales in all the flames.

3.2. Description of flame structure

3.2.1. Visible heights and flame base

Visible heights for all the flames studied are quantified and shown in Table 3. Mean flame heights are defined following the methodology of Zukoski [26], with a 50% flame intermittence criterion employed. Videos of the flames were taken at 50 Hz for 120 s resulting in 6000 images used to approximate the mean flame height. The individual video frames are binarized and then averaged temporally to produce a probability distribution of the flame intermittence.

To understand the role of diffusion and entrainment forces on the overall flame structure, DSLR images are taken of the flame neck region for each flame studied from Table 1, with an example of instantaneous images presented in Fig. 5. The transition point from a blue flame to a yellow flame nominally corresponds to the onset of soot particle formation. It is observed that with increasing levels of fuel-turbulence, the flame luminosity and structure change at the flame neck. The changes observed are solely a property of the turbulence level independent of HRR ($\dot{Q}$) and not due to the minor increases in Reynolds numbers.

Table 3
50% intermittent mean flame heights.

Flame	L_f (m)
F1	0.52
F2	0.55
F3	0.67
F4	0.76
F5	0.82

Under increased fuel-turbulence levels, the axial location for the onset of soot formation changes where the blue region extends further downstream, however, some sooting also occurs in this region as observed by streaks of yellow noted in flames F4 and F5. The delayed onset of sooting suggests that increased fuel-turbulence levels reduce soot residence times, therefore reducing soot formation close to the burner exit plane. It is also important to highlight that F1 shares similar qualitative characteristics to F2 even though the relative fuel-turbulence is double from F1 to F2. This is due to both flames having low absolute levels of fuel-turbulence, whereas F3 to F5 have much larger absolute levels of fuel-turbulence (see Table 2). This suggests that the turbulence intensity at the burner exit plane has a strong effect on the soot formation, given the visual differences between all the flames. Another important observation is that flame F5 lies at the lift-off limit, with partial lifting occurring occasionally. These observations serve as a prelude for the quantitative analysis obtained from the high-speed imaging. They also reinforce the capacity of the burner to control the mechanism of oxidiser transport into the pre-neck region of flame, which influences soot formation and oxidation.

Simultaneous measurements of OH fluorescence and Mie scattering of soot are taken for a portion of the flame length between 0–250 mm (x/D = 0–7.14) above the burner exit plane. This region is preferable for this analysis as the boundary condition at the burner exit plane defines the global flame structure [32]. A comparison of the characteristic flame structure from x/D = 0–7.14 for increasing fuel-turbulence is shown on the instantaneous exemplar images in Fig. 6. Each window shown spans an axial distance of x/D = 1.43 (50 mm). Corresponding DSLR images of the flame are shown next to the high-speed OH-PLIF and scattering images. Measurements of OH and soot for each axial window are recorded simultaneously. The soot and OH-PLIF signal intensities vary along the flame axis, however, for clarity in visualising the overall flame structure, the colour scales have been normalized to the maximum intensity in each axial measurement window. Images are obtained at a rate of 250 Hz for 20 s duration, with a total quantity of 5000 images taken of OH-PLIF and soot scattering respectively for each flame. Superimposing the high-speed images of soot and OH in a time series reveals the temporal joint evolution of soot and OH layers marking the reaction zones.

Flame F1 shown in Fig. 6a,b (lowest turbulence) will be used to describe the overall flame structure, which will be compared to Fig. 6c,d (higher turbulence) to highlight the effect of the fuel-turbulence level on the overall flame structure. For flame F1, immediately above the burner rim where the flame is stabilized, is a region (x/D = 0–1.43) that is defined by a near-laminar flame sheet. The flame front in this region is almost completely vertical, and no soot scattering is measured. There is little perturbation or curvature associated with the OH layers, indicating that the transport mechanisms into the reaction zone are diffusion-controlled. Further downstream of the flame stabilization zone, the onset of the classic flame puffing phenomena occurs at the flame neck (x/D ~ 1.43–2.86) [33]. Here, the periodic puffing motion of the flame generates toroidal vortices in a large symmetric plume that facilitates air entrainment into the flame as the vortices dissipate during the rollover of the plume. These periodic motions occur along the flame axis, with the size of the toroidal vortices increasing as

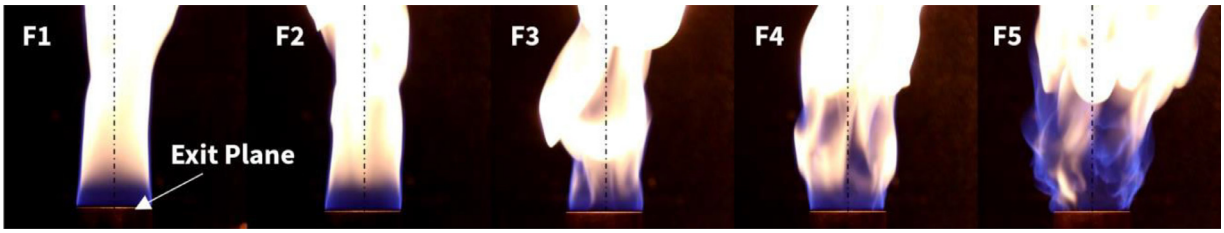

Fig. 5. Instantaneous DSLR images showing the onset of soot formation and oxidation near the burner exit plane for all flames with increasing fuel-turbulence.

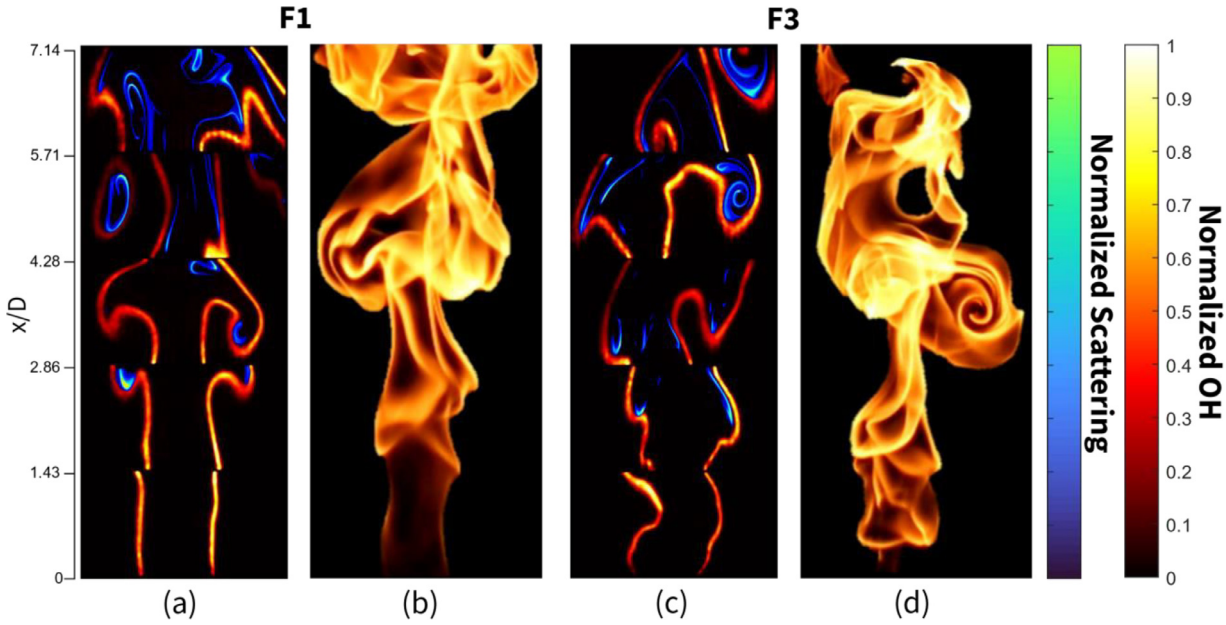

Fig. 6. (a,c) Superimposed instantaneous images of OH-PLIF (hot red colourmap) and Mie scattering of soot (cold blue colourmap) for flame 1 (F1) and flame 3 (F3). (b,c) Corresponding time-independent instantaneous DSLR images of the flames at the same scale as the high-speed images.

they are advected downstream. The high-speed imaging of OH and soot scattering reveals the occurrence of a highly periodic flame pinch-off instability, which hitherto has not been characterised in buoyant turbulent fires before and will be discussed in the proceeding section.

The series of stacked images on the right (Fig. 6c,d) shows flame F3, with increased fuel-side turbulence generated by the perforated plate. The fuel-turbulence is approximately 0.918 m/s (Table 2). It is apparent from both the laser and DSLR imaging that the addition of fuel-side turbulence strongly affects the flame structure. At the flame stabilisation zone ($x/D = 0$–1.43), the flame, which is stabilised on the burner rim, is wrinkled considerably due to the sheared flow at the exit plane. This creates asymmetric buoyancy effects along the flame length, which is observed by a large curvature of the OH sheets. It is also interesting to note that soot formation occurs further upstream compared to the less turbulent case. The influence of raising the fuel-turbulence level on entrainment forces is pronounced in the third axial measurement window ($x/D = 2.86$–4.28). Here, the symmetrical plume and distinct puffing motion have been replaced by an asymmetric vortex structure in a plume. It appears that entrainment forces are stronger, and act primarily on a single side of the flame sheet. The plume structure experiences an asymmetric rollover motion that breaks the base flame structure into an assortment of flamelets.

3.2.2. Flame pinch-off instability at the flame neck

High-speed imaging of OH-PLIF and soot scattering imaging reveals the periodic occurrence of a flame pinch-off instability occurring at the flame neck for all flames. Examples are shown in Fig. 7. Flame pinch-off refers to the separation of the main flame body at the flame neck resulting in the formation of a detached pocket flame that is advected downstream [34]. This detachment is associated with a periodic break or partial extinction/quenching occurring at the flame neck; buoyancy forces are responsible for flame oscillations that ultimately separate the flame [35]. Pinch-off instabilities are typically studied using laminar flickering jet diffusion flames by imposing acoustic forcing on the inlet jet boundary condition to phase-lock the periodic flame oscillations. This creates a resonant effect where significant vorticity that enhances entrainment from cold air is generated [35]. As the modulated frequency approaches the resonant frequency, the flame neck elongates and there is a marked increase in the pinch-off occurrence frequency [36,37]. Pinch-off instabilities formed under these conditions are symmetric and possess a varicose structure.

Intermittent pinch-off of the buoyant flames studied are observed to occur within a spectrum between two distinct modes based on the fuel-turbulence level, which consist of, (i) a varicose mode characterised by a symmetric flame neck and plume structure, (ii) a sinuous mode characterised by an asymmetric flame

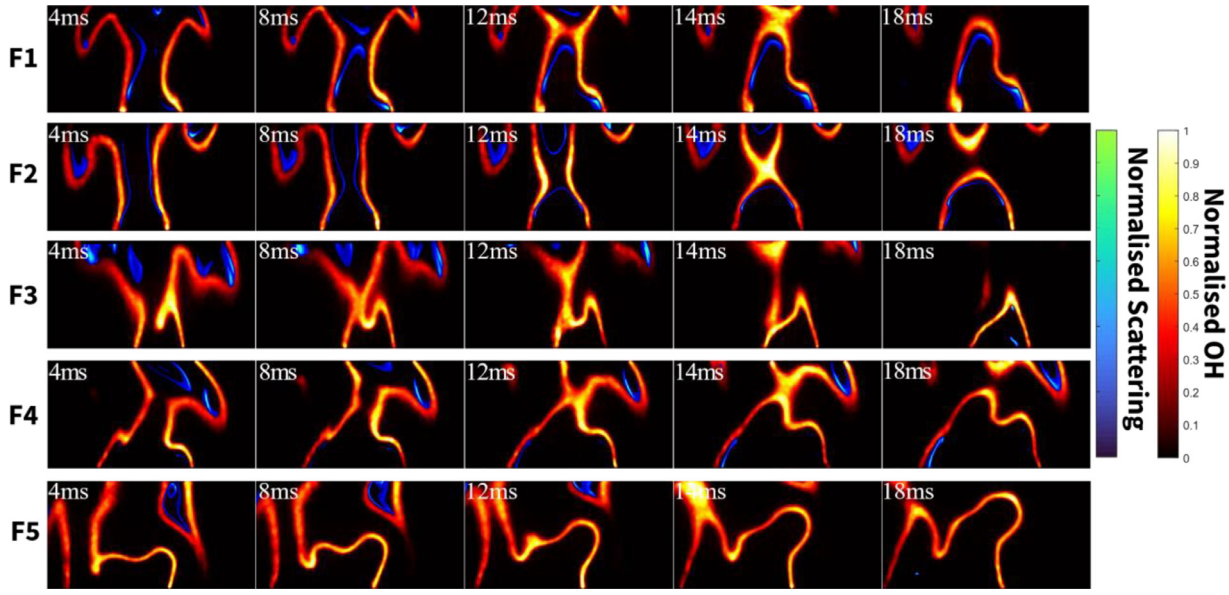

Fig. 7. Superimposed OH and Scattering time evolution of flame pinch of events from F1 (top)–F5 (bottom). Images are taken at the third axial window ($x/D = 2.85$–4.28).

neck and plume structure. Descriptions of these instabilities have been provided by Cetegen and Dong [38] for buoyant diffusion flames. However, only varicose instability modes are observed at the flame neck, similar to the laminar jet flame experiments described earlier. The low turbulence flame (F1) demonstrates the same type of varicose structures at the flame neck. However, it is observed that by raising the fuel-turbulence level, flame pinch-off is instead increasingly characterised by a sinuous motion. This occurs due to the perturbations along the flame neck that arise from the introduction of lateral angular entrainment forces.

The effect of fuel-turbulence on the pinch-off instability mode and formation time sequence for each flame at increasing levels of turbulence can be observed from the exemplar images in Fig. 7. Each exemplar image corresponds to approximately 4 ms time increments (left to right) for flames F1 to F5. F1 and F2 (low absolute turbulence levels) show the same varicose pinch-off instability mode, characterised by a symmetric flame neck and twin vortices developing between $x/D = 2.85$–4.28 that is responsible for the excessive straining and quenching of the flame neck at the instant of pinch-off. The measurements show that pinch-off occurs within a very narrow temporal window. Both flames F1 and F2 are qualitatively indistinguishable from one another due to having low absolute turbulence levels (0.135–0.283 m/s respectively). After pinch-off, the pocket flame is advected downstream out of plane within this timeframe. With increasing fuel-turbulence, there is an increasingly warped flame neck region as opposed to the classical symmetric plume structure found in the low turbulence case (F1 and F2). This is the flame shifting towards the sinuous pinch-off instability mode which causes flame oscillations that can shift both in and out of the laser sheet. The warped flame results in asymmetric “flame pocket” structures that significantly increase the entrainment rate into the pocket which further stretches the flame neck. At sufficiently large stretch rates, localised quenching occurs in the form of a sinuous pinch-off mode at the flame neck.

Example schematics of both the varicose and sinuous instability modes are provided respectively in Fig. 8 which corresponds to flame F1 and Fig. 9 which corresponds to flame F4. Both modes are shown to be defined by the angle of the entrained flow relative to the gravity vector. This angle is known to control the acceleration of entrained air into the flame, which therefore regulates the entrainment strength required to overcome the thermal expansive and diffusive forces at the flame neck. If the entrained flow velocity is large, the flame neck experiences local strain. In the purely buoyant case, the entrainment vector is almost orthogonal to gravity and the flame neck axis, which squeezes the flame neck symmetrically from both sides resulting in local quenching. This is driven by the entrainment vector overcoming the vertical buoyancy component that leads to flame stretching. For F1 (Fig. 6) this process occurs periodically as the entrainment vector is primarily controlled by the symmetric eddies in the downstream plume that results in the classical puffing motion. This phenomenon has been thoroughly characterised through joint high-speed OH-PLIF/PIV measurements by Ahn et al [37]. They also suggest that separation at the flame neck occurs due to excessive straining that results in the formation of a stagnation point between the flame base and advected flame pocket. These results appear to show that the symmetric nature of flame pinch-off is linked to the classical buoyant puffing instability.

Upon increasing fuel-turbulence, significant asymmetries are introduced into the flame neck region. The illustrative PLIF-OH images for F4 (Fig. 9) show that air is entrained into the flame neck at an acute angle relative to the gravity vector leading to the asymmetric neck structure. The observed shift from the varicose to sinuous instability mode at the flame neck region is unique for buoyant flames as this transition is typically observed significantly downstream once the flame is fully turbulent [38,39]. However, in this case, the modification of the fuel-turbulence level enables this transition to occur very close to the burner exit plane, with no symmetric flame neck forming. The sinuous pinch-off structure is driven by asymmetric flame deformation and large orientation angles, which enables a greater air entrainment vector that is imposed on one side of the flame wall than the other. This is visualised in Fig. 9, which shows the OH branch established well inside of the flame neck due to strong angular entrainment forces quenching the flame. This creates a new pathway for air entrainment into the separated flame at the same acute angle, which enables downstream advection of the flame pocket. This pinch-off mode inhibits the capacity for the flame downstream to undergo periodic buoyant motions as a distinct puffing instability cannot form. The images show that the oxidiser transport mechanism into the overall flame structure is entirely driven by angular entrainment at the local flamelet level and is dramatically different to the low turbulence buoyant flame (F1), which is entirely driven by periodic motions.

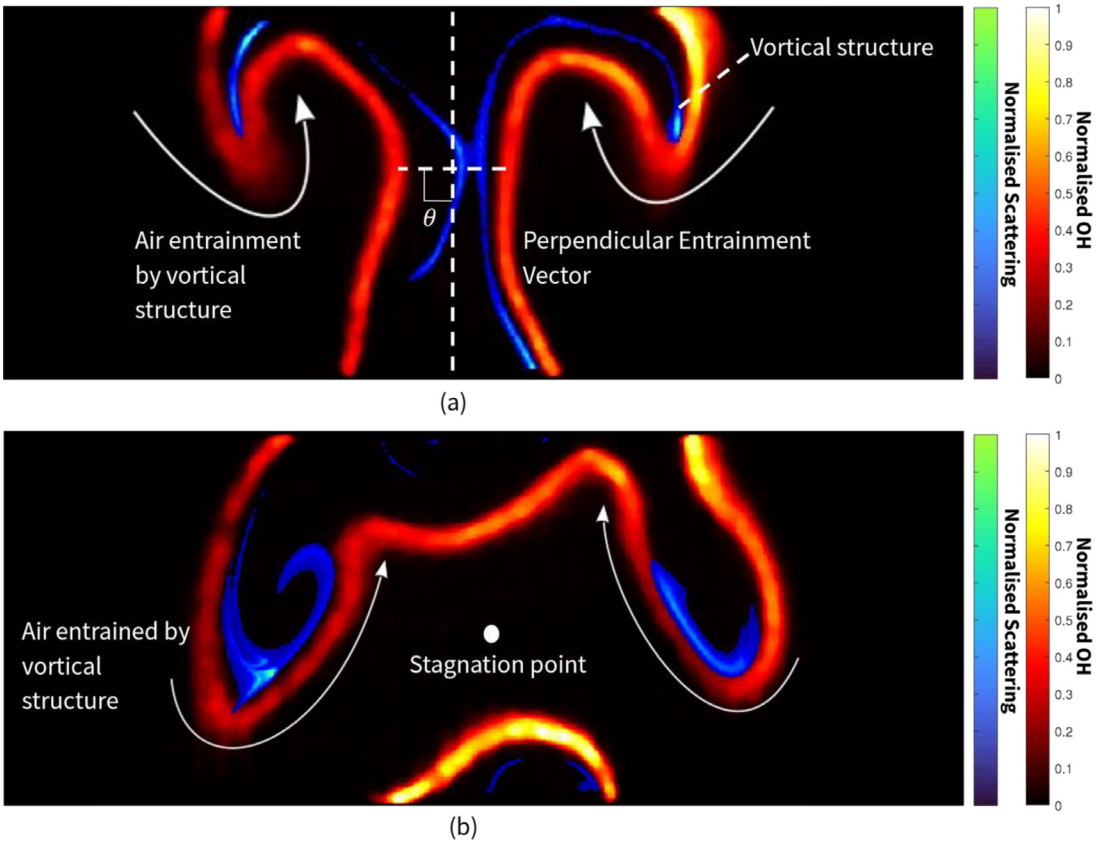

Fig. 8. Illustrations of air entrainment flow patterns under the instability mode of low fuel-turbulence (F1), whereby local quenching by air entrainment of a symmetrical flame neck leads to a pinch-off. PLIF-OH (Hot red) and Mie scattering of soot (Jet blue) intensities have been normalised for visual clarity. The annotated arrows showing the entrainment directions are intended to be solely illustrative.

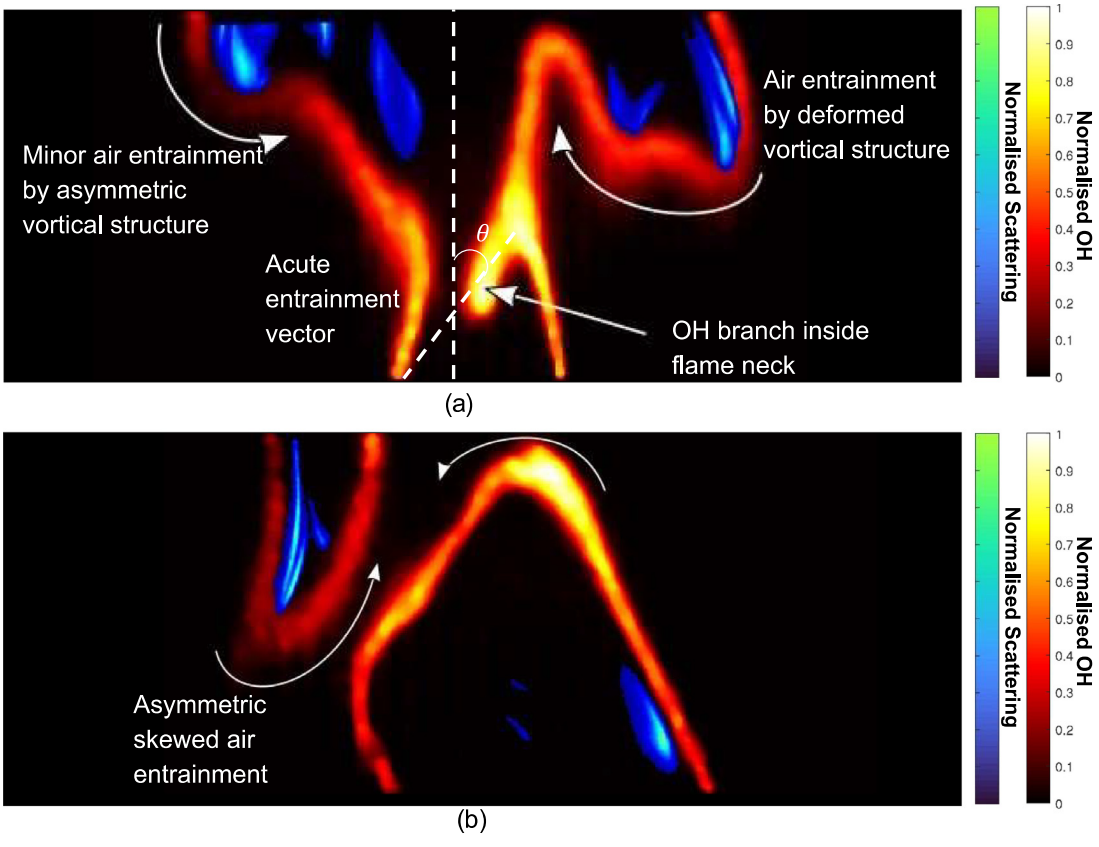

Fig. 9. Illustrations of air entrainment flow patterns under the instability mode of increased fuel side turbulence (F4). PLIF-OH (Hot red) and Mie scattering of soot (Jet blue) intensities have been normalised for visual clarity. The annotated arrows showing the entrainment directions are intended to be solely illustrative.

4. Flame structure analysis

4.1. Temporal evolution

The temporal evolution of the flame structure and fluctuating quantities are analysed using high-speed (250 Hz) signals of OH-PLIF and Mie scattering of soot. Characteristic samples of the temporally resolved signals of the binarized Mie scattering and the corresponding flame thickness at the flame neck region are shown in Fig. 10. These signals are extracted from the flame neck region ($x/D = 1.43$–2.86), where flame puffing and pinch-off instabilities occur. Soot scattering is analysed by integrating rows of the binarized image centred at $x/D = 2$, with a narrow height of 10 pixels. The flame width is quantified by approximating the distance between the skeletonized flame sheets extracted from the OH-PLIF images at the single pixel row near $x/D = 2$. The signals for each quantity are measured over a 20 second period at 250 Hz (5000 images). The frequency spectra for each flame case are obtained by employing a Fast-Fourier Transform (FFT) algorithm on the time series data for both signals. The region of interest selected for the spectral analysis is deliberate as the flame neck region defines the onset of turbulence-driven perturbations in the flame. Therefore, strong spectral responses that characterise the turbulent fluctuations of the flame are expected. This is confirmed by the spectral response of the flames, as shown in Fig. 10(b). In the absence of induced turbulence (F1), a distinct spectral line is identified at approximately 6 Hz for both the soot scattering and flame width spectra. This is the fundamental frequency of the flame, that matches the classical puffing phenomena expected for buoyant oscillatory flames. This result aligns remarkably well with the well-established $D^{-1/2}$ scaling relationship by Cetegen and Ahmed [40] and Hamins [41] in Eq. (6).

$$f = 1.5D^{-1/2} \tag{6}$$

Table 4
Puffing frequencies and cross-correlations of the flames.

Flame	Peak Frequency f_p (Hz)	Cross-Correlation Coefficient σ
F1	5.70	0.648
F2	6.10	0.664
F3	7.10	0.604
F4	6.60	0.552
F5	6.10	0.371

where D is the characteristic burner diameter (35 mm). The puffing frequency carries little dependency to $\dot{Q}$ for the flames as shown in Table 4. Both the flame width and scattering signals are closely correlated, suggesting that soot formation on the high-temperature rich side of the flame occurs as the flame widens and undergoes a “puffing” instability sequence observed by the periodic toroidal vortex structure shown in Fig. 6.

Increasing the fuel-turbulence level elicits a disparate spectrum, with a considerably flatter spectral response. A fundamental frequency becomes more difficult to extract with increasing levels of fuel-turbulence (F1 to F5). The peak (albeit convoluted) signal is interpreted to vary between 5.7–7.1 Hz depending on the flame; however, no identifiable correlation is found between the different flames. The increasingly flat spectra demonstrates the role of air entrainment and local flame stretching and quenching on the temporal flame structure. The disappearance of a fundamental puffing frequency from the spectra from flames F2–F5 highlights how large periodic eddy structures typical for small buoyant flames are eliminated resulting in a highly deformed flame structure.

The cross-correlation of soot scattering and flame width is shown in Table 4. The large cross-correlation coefficient of these quantities shows that temporal variations in the physical structure of the flame are closely related to the presence of soot. This is particularly relevant at low fuel-turbulence levels, where buoyant

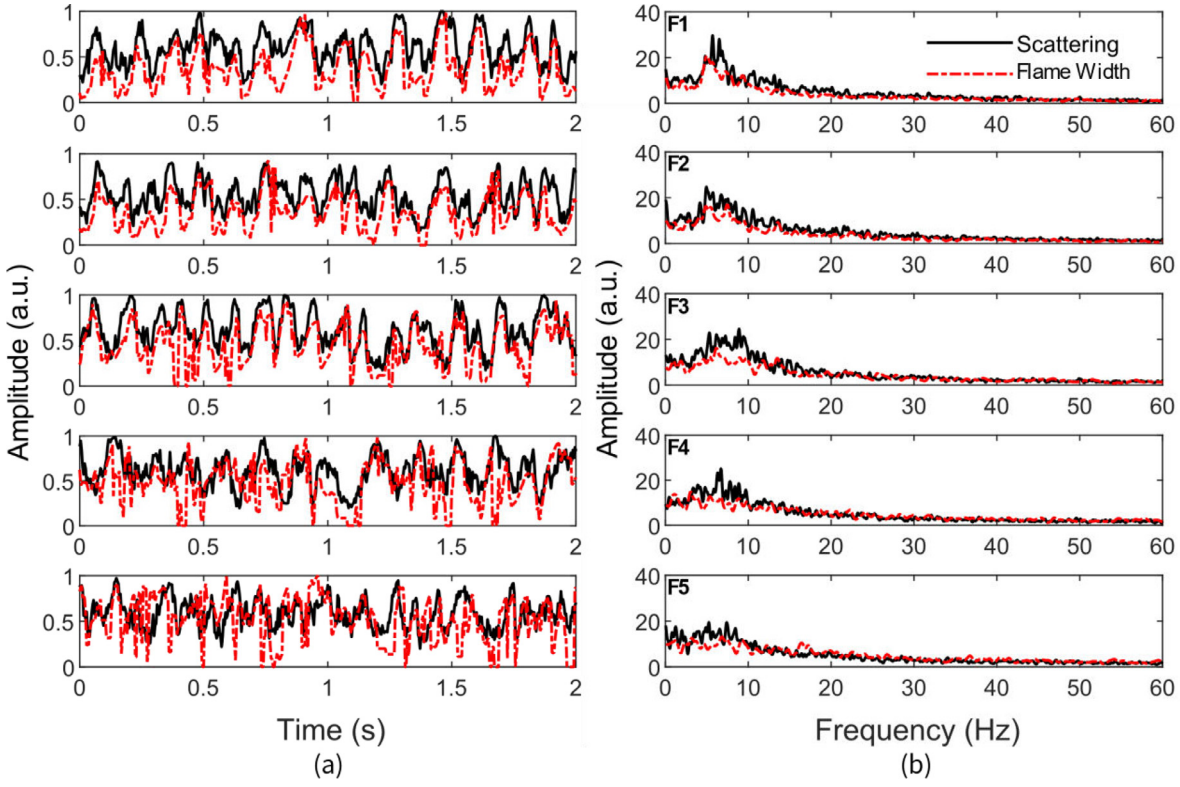

Fig. 10. Frequency response of flame width and integrated scattering signal (b) with the corresponding first 2 s of the time evolution of flame width and scattering area (a) for all the flames (F1-F5).

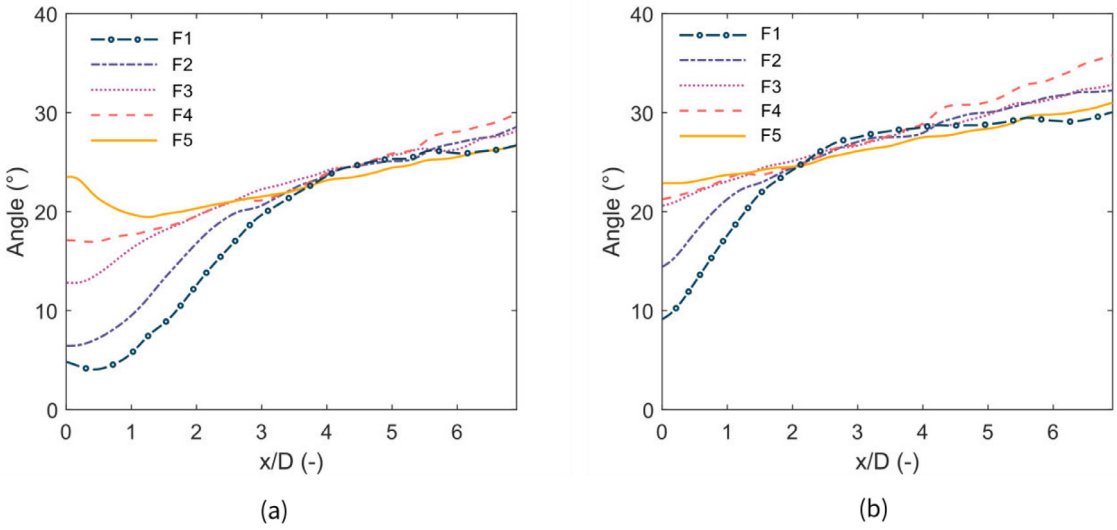

Fig. 11. Mean (a) and RMS (b) of angular deviations of skeletonized OH layers with respect to the gravity vector for all the flames.

puffing instabilities are dominant and the images from F1 (Fig. 8b) reveal that soot generally coalesces in regions of high vorticity. F1 and F2 have low absolute turbulence intensities (0.135 m/s and 0.283 m/s respectively), which correspond to similar correlation coefficients. Higher turbulence levels increasingly disrupt this process by breaking the formation of symmetrical 'puffing' through highly angled entrainment vectors, which in turn reduces the correlation between flame width and soot scattering. This suggests that either, there is an increase in soot oxidation or that soot formation is reduced due to smaller residence times within the flame neck region by increasing fuel-turbulence.

4.2. Flame orientation

The spatial structure of the flame is characterised and used to identify the onset of turbulence and the wrinkling break-up of the flame. This is quantified by extracting the mean and rms angular orientations of the OH layer relative to the vertical gravity vector shown in Fig. 11. This is done by first binarizing the OH images at a threshold of 5% of the maximum intensity of OH, then the binarized images are skeletonized. At each point on the skeleton, a centred window of 5 pixels (2 points before and 2 points after the pixel of interest) is used to approximate the angular orientation of the skeleton. The orientation angle is not sensitive to the size of the interrogation windows used. This is done along the entire length of the skeleton to obtain a distribution of angular orientations along the OH layer. The OH orientations are established with respect to the vertical axis and temporally averaged. The angular orientation of the OH layer is intended to provide insight into the role of entrainment forces acting on the flame from the air side.

For all the flames (F1–F5), at the exit plane of the burner ($x/D < 0.5$), both the mean and rms orientation angles increase monotonically with fuel-turbulence. This trend is expected as the Reynolds number is greatest at the burner exit plane. Due to the strong inertial forces, angular perturbations are the smallest near the burner exit plane and transport into the flame is diffusive. Between $x/D = 0.5$–3.5, the mean OH layer angle for the varying flames increases dramatically but eventually converges towards approximately 22° between $x/D \approx 3$–3.5. Correspondingly, the rms angles also converge between $x/D \approx 2$–2.5. The large angular perturbations in this region suggest that lateral entrainment forces are increasingly promoted below the flame neck from F1 to F5. The convergence of the flame orientation angles between $x/D = 3$–3.5 marks the transition to a buoyancy-driven flow. The angular orientations remain converged for all flames but increase linearly downstream at each axial position of x/D. The convergent nature of all the flames suggests a loss of turbulence memory as the flame develops downstream. Despite the dominance of buoyancy, the asymmetric perturbations and sinuous pinch-off instabilities in the flame neck region increasingly inhibit the formation of periodic puffing instabilities, as discussed earlier. Instead, the flame is deformed at the flame neck and this leads to a complete breakup into flamelets further downstream.

The magnitude and perturbations of the flame neck control whether varicose or sinuous pinch-off instabilities form. Once fuel-turbulence is introduced and increased, the shearing of the fuel stream facilitates lateral angular entrainment below the flame neck, leading to large flame perturbations, which force the sinuous pinch-off instability that drives the flame breakup process.

4.3. Flame front curvature

The preceding analysis has shown that increased fuel-turbulence in the near field has the effect of promoting lateral entrainment, thereby initiating pinch-off events resulting in flame break-up that marks the transition to turbulence. The onset of flame puffing and wrinkling are analysed by calculating the local flame front curvature from the binarized and skeletonized OH-PLIF images. This approach is normally undertaken for premixed turbulent flames [42], however, it is expected that as the turbulent structures such as vortices and asymmetric wrapping become more prominent, the local flame curvature increases. From the skeletonized data for each of the 5000 images, a cubic spline is fit to each $x(s)$ and $y(s)$ coordinate along the skeleton path **s**. The local curvature κ along the skeleton path is computed using Eq. (7) [43].

$$\kappa = \frac{\dot{x}\ddot{y} - \dot{y}\ddot{x}}{\left(\dot{x}^2 + \dot{y}^2\right)^{\frac{3}{2}}} \tag{7}$$

The temporal and spatial evolution of the local curvature is presented in the form of probability density functions (PDF) in Fig. 12, which shows the curvature PDF compiled from 5000 images for each interrogation window (representing the spatial coordinate x/D). The results that both F1 and F2 exhibit narrowband distributions of curvature close to the exit plane. This is consistent with the near-vertical laminar flame sheets observed in Fig. 6a. This distribution broadens for F2 at both 0 mm and 50 mm above the burner exit plane, which results from the 100% increase in fuel-turbulence levels and starts to wrinkle the laminar flame front.

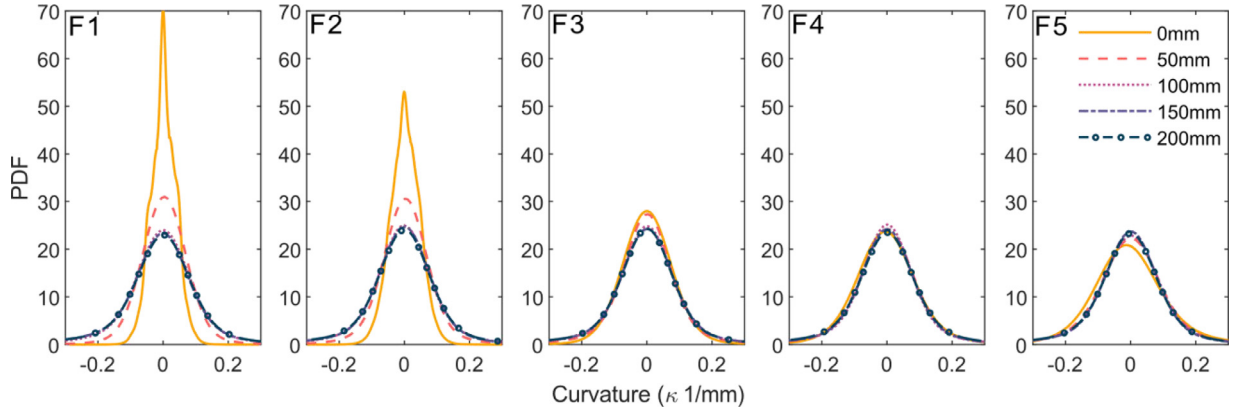

Fig. 12. Curvature PDFs of skeletonized OH layers for F1-F5 at each axial window (50 mm traverse distance).

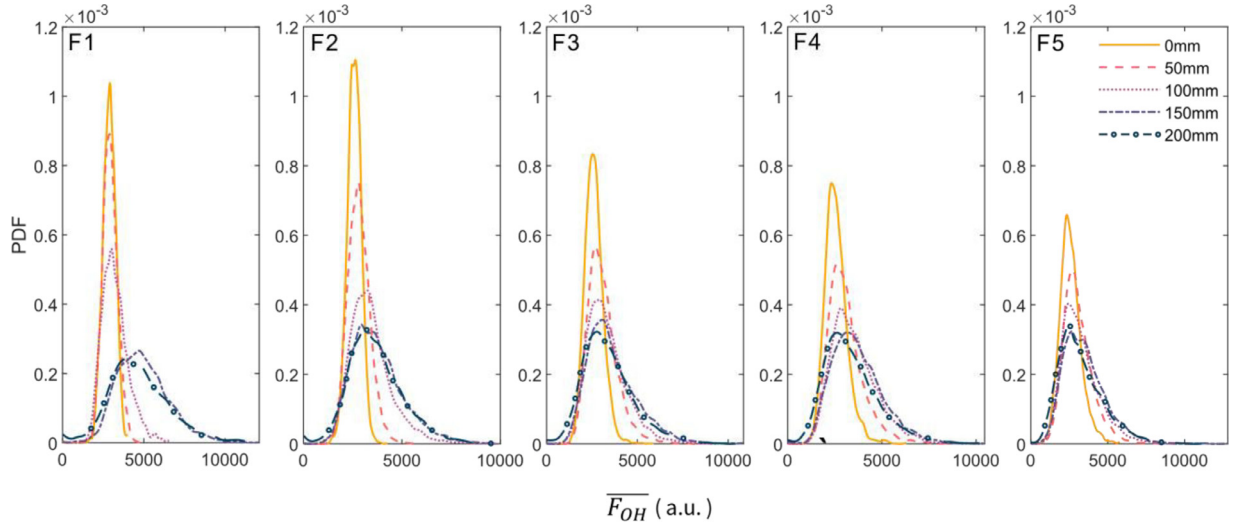

Fig. 13. Normalized OH spatial presence distribution probability density functions for F1-F5 at each axial window for the 5000 acquired images.

This is due to the 100% increase in fuel side turbulence levels wrinkling the flame front. As the fuel-turbulence level is increased from F1 to F5, the PDFs near the exit plane (0–50 mm) broaden considerably, clearly showing that increased fuel-turbulence promotes flame front wrinkling. Interestingly, curvature continually increases even to a point where curvature at the exit plane seems to be greater than that downstream of the flame (F5). Beyond 100 mm (x/D = 2.86), all the PDFs regardless of fuel-turbulence levels collapse towards a single distribution, suggesting that this region from 100–150 mm marks the transition towards buoyancy-driven turbulence defined by large vortical structures that possess large curvature. It should be noted that this transition region effectively corresponds to where pinch-off and puffing instabilities first occur (Fig. 6 at x/D 2.86). This shows a clear demarcation of axial boundaries whereby the flame transitions from a laminar diffusion regime to a buoyancy-driven turbulence regime.

4.4. Distribution of OH intensity

Both the spatial distribution and intensity of the OH signal are primarily defined by the local strain rate and fuel-turbulence. To understand how these quantities vary spatially and temporally, they are coupled to create a normalised OH intensity parameter, $\overline{F_{OH}}$, which effectively marks the flame surface area normalised by the OH intensity in each image. PDFs of this parameter are presented at each axial window for flames F1–F5. The PDFs are calculated following Eq. (8) where a 5% threshold is first applied to the OH images. In other words, the OH signal included in the calculation of $\overline{F_{OH}}$ is conditioned by the presence of the flame sheet. Images are then normalised and integrated spatially. This method is similar to a spatially averaged presence index proposed by Franzelli et al [44].

$$\overline{F_{OH}} = \sum_{i=1}^{n_x}\sum_{j=1}^{n_x} F_{OH}/F_{OH_{max}} \tag{8}$$

PDFs of $\overline{F_{OH}}$ for F1–F5 at each axial window is presented in Fig. 13. The parameter $\overline{F_{OH}}$ effectively marks the spatial presence and intensity of the OH signal at a given measurement location. As observed from instantaneous images (Fig. 6), the OH signal possesses a greater spatial occupation area in the image as the axial length increases due to the formation of buoyant instabilities followed by the break-up of the flame. The PDFs confirm this trend, with more narrow distributions observed across F1–F5 from 0–100 mm. It is interesting to note that the PDFs at 0 mm, 50 mm, and 100 mm (except for F1 at 0 mm) continuously broaden with increasing fuel-turbulence. This shows that the flame surface area monotonically increases due to the introduction of flame wrinkling promoted by lateral entrainment earlier in the diffusion-dominated “jet” component of the flame. Further downstream from 150–200 mm, the PDFs asymptotically collapse to a singular PDF with increasing axial distance, marking the location where buoyancy-driven turbulence completely dominates the flame structure. Quantitative measurements of the velocity and

temperature in the downstream region of the flames are key to understanding the role of fuel-turbulence generation on the overall flame properties. These measurements will be carried out in a future study.

5. Summary and conclusion

This paper presents the characterisation of a novel canonical burner that enables the study of buoyant flames with controlled levels of fuel-turbulence. This is achieved by using a recessed perforated plate that raises the turbulent velocity fluctuations at the burner exit plane from 0.135–1.813 m/s. Integral time scales quantified from LDV measurements decrease with increasing turbulence while the integral length scales remain the same for all flames. It is demonstrated that the plate generates large shear in the bulk fuel flow, thereby raising the turbulent kinetic energy at the burner exit plane. The flame structure is spatially and temporally resolved by simultaneous high-speed imaging measurements of OH-PLIF and Mie scattering of soot at several locations downstream of the burner exit plane. It was shown that by raising fuel-turbulence levels:

- The angular orientation of the flame sheet in the near-field along the vertical axis increases with increasing fuel-turbulence. Fluctuations in the flow at the burner exit plane promote lateral angular entrainment into the flame neck region, leading to large flame perturbations and flame breakup.
- Probability density functions of the flame front curvature and OH intensity (marking flame surface area) increasingly broaden in the near-field region of the flame (before the puffing location) as flame wrinkling occurs resulting from lateral entrainment. The onset of the transition to buoyancy-driven turbulence also shifts more upstream.
- Puffing instabilities extracted from the high-speed measurements in the buoyant flames free from fuel-turbulence generation align closely with empirical models. Puffing instabilities are observed in all flames, with an increasingly flat spectral response with increasing fuel-turbulence. Cross correlations of the flame width and soot scattering at the flame neck decrease with increasing fuel-turbulence.
- A pinch-off instability commonly associated with buoyant pool fires has been observed to initially take place at the flame neck. This occurs due to the lateral entrainment vector, where air-side entrainment forces overcome the diffusive and thermal expansive forces in the flame sheet that quenches the flame until separation into a flame base and pocket.
- Increasing fuel-turbulence transitions the flame from a varicose to a sinuous instability. This inhibits the capacity for the flame to generate a classical puffing instability, thereby shifting the mechanism of oxidiser transport into the flame.

These results demonstrate that the burner can modify entrainment into the near-field region of the fire. This enables the burner to control key processes defining turbulent fires such as the dominant buoyant flame instabilities, turbulence-radiation interaction, and soot formation. Therefore, this work provides valuable measurements of flame structure and develops a platform for future quantitative measurements to characterise buoyancy-turbulence interactions and help further develop and validate numerical models.

Declaration of Competing Interest

The authors declare that they have no known competing financial interests or personal relationships that could have appeared to influence the work reported in this paper.

Acknowledgement

This work is supported by the Australian Research Council (DP200103609).

Supplementary materials

Supplementary material associated with this article can be found, in the online version, at doi:10.1016/j.combustflame.2023.112993.

References

[1] S.R. Tieszen, On the fluid mechanics of fires, Annu. Rev. Fluid Mech. 33 (2001) 67–92.
[2] L. Audouin, G. Kolb, J.L. Torero, J.M. Most, Average centreline temperatures of a buoyant pool fire obtained by image processing of video recordings, Fire Saf. J. 24 (1995) 167–187.
[3] A. Hamins, M. Klassen, J. Gore, T. Kashiwagi, Estimate of flame radiance via a single location measurement in liquid pool fires, Combust. Flame 86 (1991) 223–228.
[4] P.H. Thomas, The size of flame from natural fires, Proc. Combust. Inst. 9 (1963) 844–859.
[5] L. Orloff, J. De Ris, M.A. Delichatsios, Radiation from buoyant turbulent diffusion flames, Combust. Sci. Technol. 84 (1992) 177–186.
[6] G. Maragkos, B. Merci, On the use of dynamic turbulence modelling in fire applications, Combust. Flame 216 (2020) 9–23.
[7] G. Maragkos, T. Beji, B. Merci, Advances in modelling in CFD simulations of turbulent gaseous pool fires, Combust. Flame 181 (2017) 22–38.
[8] E. Weckman, Experimental investigation of the turbulence structure of medium-scale methanol pool fires, Combust. Flame 105 (1996) 245–266.
[9] X. Ren, D. Zeng, Y. Wang, G. Xiong, G. Agarwal, M. Gollner, Temperature measurement of a turbulent buoyant ethylene diffusion flame using a dual-thermocouple technique, Fire Saf. J. 120 (2021) 103061.
[10] S.P. Kearney, T.W. Grasser, Laser-diagnostic mapping of temperature and soot statistics in a 2-m diameter turbulent pool fire, Combust. Flame 186 (2017) 32–44.
[11] D. Zeng, P. Chatterjee, Y. Wang, The effect of oxygen depletion on soot and thermal radiation in buoyant turbulent diffusion flames, Proc. Combust. Inst. 37 (2019) 825–832.
[12] Y. Xin, J.P. Gore, Two-dimensional soot distributions in buoyant turbulent fires, Proc. Combust. Inst. 30 (2005) 719–726.
[13] K. Frederickson, S.P. Kearney, A. Luketa, J.C. Hewson, T.W. Grasser, Dual-pump CARS measurements of temperature and oxygen in a turbulent methanol-fueled pool fire, Combust. Sci. Technol. 182 (2010) 941–959.
[14] K. Frederickson, S.P. Kearney, T.W. Grasser, Laser-induced incandescence measurements of soot in turbulent pool fires, Appl. Opt. 50 (2011) A49.
[15] J.P. White, E.D. Link, A.C. Trouvé, P.B. Sunderland, A.W. Marshall, J.A. Sheffel, M.L. Corn, M.B. Colket, M. Chaos, H.-Z. Yu, Radiative emissions measurements from a buoyant, turbulent line flame under oxidizer-dilution quenching conditions, Fire Saf. J. 76 (2015) 74–84.
[16] G. Xiong, D. Zeng, P.P. Panda, Y. Wang, Laser induced incandescence measurement of soot in ethylene buoyant turbulent diffusion flames under normal and reduced oxygen concentrations, Combust. Flame 230 (2021) 111456.
[17] A. Hamins, T. Kashiwagi, R. Buch, Characteristics of pool fire burning, Fire Resist. Ind. Fluids, ASTM International, 100 Barr Harbor Drive, PO Box C700, West Conshohocken, PA 19428-2959, 1996 15-15–27.
[18] A. Luketa, T. Blanchat, The phoenix series large-scale methane gas burner experiments and liquid methane pool fires experiments on water, Combust. Flame 162 (2015) 4497–4513.
[19] A. Brown, M. Bruns, M. Gollner, J. Hewson, G. Maragkos, A. Marshall, R. McDermott, B. Merci, T. Rogaume, S. Stoliarov, J. Torero, A. Trouvé, Y. Wang, E. Weckman, Proceedings of the first workshop organized by the IAFSS Working Group on Measurement and Computation of Fire Phenomena (MaCFP), Fire Saf. J. 101 (2018) 1–17.
[20] J.L. Torero, Scaling-up fire, Proc. Combust. Inst. 34 (2013) 99–124.
[21] Y. Chen, J. Fang, X. Zhang, Y. Miao, Y. Lin, R. Tu, L. Hu, Pool fire dynamics: principles, models and recent advances, Prog. Energy Combust. Sci. 95 (2023) 101070.
[22] N. Wu, G. Kolb, J.L. Torero, Piloted ignition of a slick of oil on a water sublayer: the effect of weathering, Symp. Combust. 27 (1998) 2783–2790.
[23] Y. Zhang, M. Kim, P.B. Sunderland, J.G. Quintiere, J. de Ris, A burner to emulate condensed phase fuels, Exp. Therm. Fluid Sci. 73 (2016) 87–93.
[24] M.A. Delichatsios, Transition from momentum to buoyancy-controlled turbulent jet diffusion flames and flame height relationships, Combust. Flame 92 (1993) 349–364.
[25] M.A. Delichatsios, Air entrainment into buoyant jet flames and pool fires, Combust. Flame 70 (1987) 33–46.
[26] E.E. Zukoski, T. Kubota, B. Cetegen, Entrainment in fire plumes, Fire Saf. J. 3 (1981) 107–121.

[27] M. Juddoo, A.R. Masri, High-speed OH-PLIF imaging of extinction and re-ignition in non-premixed flames with various levels of oxygenation, Combust. Flame 158 (2011) 902–914.
[28] S.M. Soloff, R.J. Adrian, Z.C. Liu, Distortion compensation for generalized stereoscopic particle image velocimetry, Meas. Sci. Technol. 8 (1997).
[29] J. Kühnen, D. Scarselli, M. Schaner, B. Hof, Relaminarization by steady modification of the streamwise velocity profile in a pipe, Flow, Turbul. Combust. 100 (2018) 919–943.
[30] Y.C. Chen, R.W. Bilger, Turbulence measurements on a bunsen burner inserted with perforated plugs of different hole sizes using DPIV, Exp. Therm. Fluid Sci. 27 (2003) 619–627.
[31] H. Nobach, Local time estimation for the slotted correlation function of randomly sampled LDA data, Exp. Fluids 32 (2002) 337–345.
[32] L. Ma, F. Nmira, J.-L. Consalvi, Large Eddy Simulation of medium-scale methanol pool fires - effects of pool boundary conditions, Combust. Flame 222 (2020) 336–354.
[33] T.L. Henriksen, T.A. Ring, E.G. Eddings, G.J. Nathan, Puffing frequency and soot extinction correlation in JP-8 and heptane pool fires, Combust. Sci. Technol. 180 (2008) 699–712.
[34] C.R. Shaddix, J.E. Harrington, K.C. Smyth, Quantitative measurements of enhanced soot production in a flickering methane/air diffusion flame, Combust. Flame 99 (1994) 723–732.
[35] J. Carpio, M. Sánchez-Sanz, E. Fernández-Tarrazo, Pinch-off in forced and non-forced, buoyant laminar jet diffusion flames, Combust. Flame 159 (2012) 161–169.
[36] Y. Gao, X. Yang, C. Fu, Y. Yang, Z. Li, H. Zhang, F. Qi, 10 kHz simultaneous PIV/PLIF study of the diffusion flame response to periodic acoustic forcing, Appl. Opt. 58 (2019) C112.
[37] M. Ahn, D. Lim, T. Kim, Y. Yoon, Pinch-off process of Burke–Schumann flame under acoustic excitation, Combust. Flame 231 (2021) 111478.
[38] B.M. Cetegen, Y. Dong, Experiments on the instability modes of buoyant diffusion flames and effects of ambient atmosphere on the instabilities, Exp. Fluids 28 (2000) 546–558.
[39] H. Zhang, X. Xia, Y. Gao, Instability transition of a jet diffusion flame in quiescent environment, Proc. Combust. Inst. 38 (2021) 4971–4978.
[40] B.M. Cetegen, T.A. Ahmed, Experiments on the periodic instability of buoyant plumes and pool fires, Combust. Flame 93 (1993) 157–184.
[41] A. Hamins, J.C. Yang, T. Kashiwagi, An experimental investigation of the pulsation frequency of flames, Symp. Combust. 24 (1992) 1695–1702.
[42] A. Soika, F. Dinkelacker, A. Leipertz, Pressure influence on the flame front curvature of turbulent premixed flames: comparison between experiment and theory, Combust. Flame (2003) 132.
[43] M.S. Sweeney, S. Hochgreb, R.S. Barlow, The structure of premixed and stratified low turbulence flames, Combust. Flame 158 (2011).
[44] B. Franzelli, P. Scouflaire, S. Candel, Time-resolved spatial patterns and interactions of soot, PAH and OH in a turbulent diffusion flame, Proc. Combust. Inst. 35 (2015) 1921–1929.